# The Seasonality and Interannual Variability of Arctic Sea Ice Reemergence

Mitchell Bushuk

*Atmospheric and Oceanic Sciences Program, Princeton University, Princeton, New Jersey, and Courant Institute of Mathematical Sciences, New York University, New York, New York*

Dimitrios Giannakis

*Courant Institute of Mathematical Sciences, New York University, New York, New York*

(Manuscript received 26 July 2016, in final form 24 February 2017)

## ABSTRACT

There is a significant gap between the potential predictability of Arctic sea ice area and the current forecast skill of operational prediction systems. One route to closing this gap is improving understanding of the physical mechanisms, such as sea ice reemergence, which underlie this inherent predictability. Sea ice reemergence refers to the tendency of melt-season sea ice area anomalies to recur the following growth season and growth-season anomalies to recur the following melt season. This study builds on earlier work, providing a mode-based analysis of the seasonality and interannual variability of three distinct reemergence mechanisms. These mechanisms are studied using a common set of coupled modes of variability obtained via coupled nonlinear Laplacian spectral analysis, a data analysis technique for high-dimensional multivariate datasets. The coupled modes capture the covariability of sea ice concentration (SIC), sea surface temperature (SST), sea level pressure (SLP), and sea ice thickness (SIT) in a control integration of a global climate model. Using a parsimonious reemergence mode family, the spatial characteristics of growth-to-melt reemergence are studied, and an SIT–SIC reemergence mechanism is examined. A set of reemergence metrics to quantify the amplitude and phase of growth-to-melt reemergence are introduced. Metrics quantifying SST–SIC and SLP–SIC mechanisms for melt-to-growth reemergence are also computed. A simultaneous comparison of the three reemergence mechanisms, with focus on their seasonality and interannual variability, is performed. Finally, the conclusions are tested in a model hierarchy, consisting of models that share the same sea ice component but differ in their atmospheric and oceanic formulation.

## 1. Introduction

Arctic sea ice extent (SIE) has declined precipitously over the satellite era at a rate of roughly $-14\%$ decade$^{-1}$ (Serreze et al. 2007; Stroeve et al. 2014). In addition to this decrease in areal coverage, submarine, satellite, and in situ measurements indicate that Arctic sea ice is becoming thinner (Rothrock et al. 1999; Kwok and Rothrock 2009), transitioning from multiyear to first-year ice (Rigor and Wallace 2004; Maslanik et al. 2011) and experiencing longer melt seasons (Perovich and Polashenski 2012; Stroeve et al. 2014). Because of the positive feedback between sea ice and surface albedo (Budyko 1969; Curry et al. 1995), these changes have potential implications for the stability of the Arctic summer sea ice pack (Lindsay and Zhang

2005; Holland et al. 2006b; Winton 2006; Maslanik et al. 2007). The reduction in sea ice thickness (SIT) crucially affects Arctic climate, as it modifies heat and momentum fluxes between the atmosphere and the ocean (Maykut 1978), which, in turn, affect the large-scale mean state and variability of the atmosphere–ice–ocean system (Holland et al. 2006a). In addition to the positive ice-albedo feedback, SIT also plays an important role in negative Arctic feedback mechanisms such as the ice thickness–ice growth rate feedback (Bitz and Roe 2004) and the ice thickness–ice strength feedback (Owens and Lemke 1990).

The recent decline in SIE has motivated interest in seasonal prediction and predictability of Arctic sea ice. Predictions made with coupled global climate models (GCMs) have skill in predicting pan-Arctic SIE at lead times of 2–6 months (Wang et al. 2013; Chevallier et al. 2013; Sigmond et al. 2013; Merryfield et al. 2013; Msadek et al. 2014; Peterson et al. 2015). These lead times are

*Corresponding author*: Mitch Bushuk, mitchell.bushuk@noaa.gov

substantially shorter than predictability estimates from "perfect model" experiments, which show that Arctic sea ice area and volume are potentially predictable for lead times of 12–24 and 24–48 months, respectively (Koenigk and Mikolajewicz 2009; Holland et al. 2011; Blanchard-Wrigglesworth et al. 2011b; Tietsche et al. 2014; Germe et al. 2014). This gap between operational and perfect model prediction skill represents the forecast skill improvements potentially achievable via improved model physics and/or initial conditions. Achieving these forecast improvements depends crucially on understanding, as well as accurately initializing and simulating, the physical mechanisms that underlie the inherent predictability of Arctic sea ice. In the present study, we focus our attention on sea ice reemergence, one such "predictability mechanism."

Owing to its persistence, SIT provides a source of predictability for the Arctic climate system (Chevallier and Salas y Mélia 2012). This is a property that could be exploited by operational sea ice prediction systems. Indeed, recent studies have shown improved prediction skill in model experiments with improved SIT initial conditions (Lindsay et al. 2012; Yang et al. 2014; Day et al. 2014a; Collow et al. 2015; Guemas et al. 2016). The SIT state also has important implications for inherent sea ice predictability, as GCM studies show that thin sea ice states are generally less predictable than thick ice states (Holland et al. 2011; Germe et al. 2014). SIT persistence in the central Arctic is also responsible for a reemergence of sea ice area anomalies that occurs between the growth season and the following melt season, despite a loss of correlation over the intervening winter months (Blanchard-Wrigglesworth et al. 2011a; Day et al. 2014b). A similar reemergence occurs between melt-season and growth-season sea ice area anomalies, which is related to sea surface temperature (SST) persistence in the seasonal-ice zones and large-scale atmospheric regime persistence (Blanchard-Wrigglesworth et al. 2011a; Day et al. 2014b; Bushuk et al. 2014, 2015; Bushuk and Giannakis 2015). These two lagged correlation phenomena have collectively been termed sea ice reemergence (Blanchard-Wrigglesworth et al. 2011a). Henceforth, we will refer to the two varieties of reemergence as growth-to-melt and melt-to-growth reemergence, respectively.

In this study, we examine sea ice reemergence in a GCM hierarchy using a mode-based perspective. We extract spatiotemporal modes of Arctic covariability using coupled nonlinear Laplacian spectral analysis (NLSA; Giannakis and Majda 2012b; Bushuk et al. 2014), a high-dimensional multivariate data analysis approach, which is independent of physical units. Coupled NLSA, as described in section 2, is applied to Arctic

sea ice concentration (SIC), SIT, SST, and SLP, and the resulting modes of variability are used to study sea ice reemergence. We use these modes to construct low-dimensional reemergence mode families, which capture the crucial lagged correlation features of reemergence in a parsimonious manner. This mode-based approach has a number of appealing features, particularly the following: 1) the mode time series allow for detailed analysis of the temporal evolution and variability of reemergence; 2) the spatiotemporal modes reveal the spatial patterns and seasonal evolution of reemerging SIC anomalies and other related physical fields; and 3) the coupled analysis provides a natural connection between Arctic SIC and large-scale modes of climate variability. We seek to leverage these strengths in this study, exploring the seasonality and interannual variability of sea ice reemergence mechanisms.

The plan of this paper is as follows. In section 2, we summarize the datasets and data analysis techniques used in this study. In section 3, we examine growth-to-melt reemergence, focusing on the mechanism proposed by Blanchard-Wrigglesworth et al. (2011a) in which growth-season (fall) SIC anomalies reemerge the following melt season (spring) as a result of persistent SIT anomalies in the central Arctic. We find that this mechanism is well represented by the reemergence family, and we study its spatial patterns, seasonal evolution, and interannual variability. This is done in a similar spirit to earlier work on melt-to-growth reemergence (Bushuk et al. 2015). In section 4, we introduce a unified view of growth-to-melt and melt-to-growth reemergence mechanisms, exploring their seasonality and interannual variability using a single mode family. We find that each reemergence mechanism has a clear relation to the seasonal cycle and displays distinct periods of activity and quiescence. In section 5, we explore these results in a hierarchy of coupled models that share the same sea ice component but differ in their atmospheric and oceanic formulation. Finally, conclusions are presented in section 6.

## 2. Datasets and methods

### a. CCSM4 experiments and observational datasets

This study is primarily based on analysis of a fully coupled 1300-yr control run (b40.1850.track1.1deg.006) of the Community Climate System Model, version 4 (CCSM4; Gent et al. 2011). This run is forced with 1850 greenhouse gas levels and has 1° nominal resolution for the ocean and sea ice components and 0.9° × 1.25° latitude–longitude resolution for the atmospheric component. CCSM4 realistically simulates many aspects of

Arctic climate and has a number of improvements compared with CCSM3 (Jahn et al. 2012). Of particular note for the present study is the significantly improved SIT representation in CCSM4, which motivates the use of this model to examine the role of SIT in growth-to-melt sea ice reemergence. The large-scale pattern of climatological SIT in CCSM4 agrees reasonably well with available observations, with thickest ice north of Greenland and the Canadian Archipelago. Notably, CCSM4 does not display the erroneous secondary SIT maximum in the Chukchi and East Siberian Seas that was present in CCSM3 (Holland et al. 2006a). The climatological seasonal cycle of pan-Arctic SIE in CCSM4 agrees well with the satellite-observed seasonal cycle. While pan-Arctic SIE is well represented, CCSM4 has regional climatological biases in SIC. In particular, the largest biases occur in September, where CCSM4 has a negative bias (too little sea ice) in the Beaufort and Chukchi Seas and positive biases (too much sea ice) in Baffin Bay, the Greenland–Iceland–Norwegian (GIN) Seas, and the Barents Sea.

We also analyze a CCSM4 climate model hierarchy, consisting of three models with identical sea ice components but differing atmospheric and oceanic formulations. Specifically, the hierarchy consists of the fully coupled model described above, a slab-ocean model (SOM), and an ice–ocean model driven by specified atmospheric forcing fields. The same model hierarchy has also been used previously in the study of melt-to-growth reemergence of Bushuk and Giannakis (2015). The SOM is the "CCSM4-NEWSOM," as documented in Bitz et al. (2012). This model shares the same formulation as the control run, except for the replacement of a full-depth ocean with a mixed layer ocean. The mixed layer depth used in the SOM is computed offline using the control run and is spatially varying but fixed in time. The SOM also has a spatially and seasonally varying "$Q$ flux" term, also computed offline, which accounts for heat flux due to oceanic heat transport convergence, an effect that cannot be directly simulated by the mixed layer ocean dynamics of the SOM. The SOM run is 60 years long and uses the same grid as the control run.

The ice–ocean model uses the same ocean and sea ice components as the control run and is forced by phase II of the Co-ordinated Ocean–Ice Reference Experiments (CORE-II) forcing fields (Large and Yeager 2009; Danabasoglu et al. 2014). We henceforth refer to this simulation as the "CORE-II run." The CORE-II forcing consists of interannually varying atmospheric surface forcing fields spanning the time period 1948–2007. The forcing fields have some state variables that are based on gridded observational products and others based on National Centers for Environmental Prediction (NCEP)–National Center for Atmospheric Research

(NCAR) reanalysis data (Kalnay et al. 1996). As detailed in Large and Yeager (2009), corrections are applied to these data in order to provide agreement with available satellite and in situ data. This time period exhibits trends associated with greenhouse gas–forced variability. To focus on the internal variability of this experiment, the data were detrended by subtracting monthly linear trends from each month.

We also analyze passive microwave satellite observations of SIC from the National Snow and Ice Data Center (NSIDC). We use the monthly averaged SIC dataset processed using the NASA team algorithm (Cavalieri et al. 2012), which is provided on a 25-km polar stereographic grid and spans 36 years (1979–2014, inclusive). We detrend the NSIDC data by subtracting monthly linear trends from each month.

All data used in this study are monthly averaged, and, crucially, the seasonal cycle has not been removed. Retaining the seasonal cycle allows us to extract "intermittent type" modes from the data, which represent the interaction of low-frequency variability with the seasonal cycle, in both space and time.

### b. Data analysis methods

In this study, we utilize the coupled NLSA algorithm, as developed in Bushuk et al. (2014), to investigate the covariability of SIC, SST, SLP, and SIT in the Arctic sector. Coupled NLSA is a multivariate generalization of the NLSA algorithm (Giannakis and Majda 2012a,b, 2013), a nonlinear data analysis technique for high-dimensional datasets. Coupled NLSA merges two key concepts: 1) the use of time-lagged embedding for time series analysis of dynamical systems (Packard et al. 1980; Broomhead and King 1986; Vautard and Ghil 1989; Sauer et al. 1991) and 2) the use of a kernel function to assess the similarity between samples of nonlinear data (Belkin and Niyogi 2003; Coifman and Lafon 2006).

Suppose $x_t$ is an $s$-sample time series of a variable defined over $d$ spatial grid points, with a uniform time step of $\delta t$ (here, $\delta_t = 1$ month). The first step of coupled NLSA is to time-lag embed all variables of interest in the higher-dimensional space $\mathbb{R}^{dq}$. Each sample in this "embedding" space represents a $q$-snapshot spatiotemporal pattern of the input data. The parameter $q$ is chosen by the user and specifies the length of these spatiotemporal patterns. In this study, we use a value of $q = 24$ months. Specifically, time-lagged embedding is performed via the following mapping:

$$x_j \mapsto X_j = [x_j, x_{j-1}, \ldots, x_{j-(q-1)}],$$

where the index $j$ represents time $t_j = t_1 + (j-1)\delta t$. Time-lagged embedding allows one to study the variability of spatiotemporal patterns and also provides

superior time-scale separation to empirical orthogonal function (EOF) analysis.

In this study, we assess the similarity between states using a pairwise kernel function defined as follows:

$$K_{ij} = \exp\left(-\frac{\|X_i^{SIC} - X_j^{SIC}\|^2}{\epsilon\|\xi_i^{SIC}\|\|\xi_j^{SIC}\|}\right) \exp\left(-\frac{\|X_i^{SST} - X_j^{SST}\|^2}{\epsilon\|\xi_i^{SST}\|\|\xi_j^{SST}\|}\right) \exp\left(-\frac{\|X_i^{SLP} - X_j^{SLP}\|^2}{\epsilon\|\xi_i^{SLP}\|\|\xi_j^{SLP}\|}\right)$$

where

$$\xi_i^{SIC} = X_i^{SIC} - X_{i-1}^{SIC},$$
$$\xi_i^{SST} = X_i^{SST} - X_{i-1}^{SST}, \quad \text{and}$$
$$\xi_i^{SLP} = X_i^{SLP} - X_{i-1}^{SLP}$$

are the velocities of each variable in lagged embedding space, and $\|\cdot\|$ is the Euclidean norm. The kernel function $K$ can be thought of as a local version of the temporal covariance matrix, which decays to zero outside of a given neighborhood. The term $K_{ij}$ provides a measure of similarity between the SIC, SST, and SLP states at times $t_i$ and $t_j$. The locality of the kernel is determined by the user-selected scale parameter $\epsilon$. For typical climate datasets $\epsilon$ is roughly 1, and smaller values of $\epsilon$ can be chosen as the number of samples increases.

The kernel function has two key features, which make it well suited for multivariate data analysis: 1) the kernel is independent of physical units, by virtue of the division by $\xi_i$, and 2) the product form of this kernel emphasizes covariability between the different input fields. In particular, obtaining a large value of $K_{ij}$ requires a simultaneous high degree of similarity between $X_i^{SIC}$ and $X_j^{SIC}$, $X_i^{SST}$ and $X_j^{SST}$, and $X_i^{SLP}$ and $X_j^{SLP}$. If any of these fields have low similarity, the value of $K_{ij}$ will be substantially reduced.

Coupled NLSA uses these kernel values to extract coupled modes of spatiotemporal variability from the input data. Using $K$, a graph Laplacian matrix is computed, and an eigenvalue problem is solved, yielding a set of Laplacian eigenfunctions. These eigenfunctions are orthonormal with respect to $\mu$, the invariant measure corresponding to the kernel $K$. The data for each variable of interest are projected onto the leading $l$ eigenfunctions, and a singular value decomposition (SVD) of the resulting "filtered" dataset is performed, yielding a set of $l$ modes of variability. Each mode consists of a $q$-snapshot spatiotemporal pattern (analogous to an extended EOF) and an associated time series (analogous to a principal component). The modes for different variables of interest are inherently coupled because the data for each variable are projected onto a common set of coupled eigenfunctions. These eigenfunctions, which are "learned" directly from the multivariate data, act as a temporal filter for the data. Note that the temporal modes are orthonormal with respect to the invariant measure $\mu$. The standard deviation of these modes is equal to one in the case of uniform measure and is slightly different from one in most climate applications. For example, in the present study, the standard deviation of the temporal modes ranges between 1.00 and 1.07. Therefore, the temporal modes from NLSA can be interpreted analogously to principal components in EOF analysis, which have unit standard deviation. We refer the reader to Bushuk et al. (2014) and Bushuk et al. (2015) for a more detailed description of the coupled NLSA algorithm.

### c. Coupled modes of variability and reemergence families

For each of the model experiments above, we use coupled NLSA to extract modes of covariability for SIC, SST, SLP, and SIT. We compute the coupled NLSA kernel using SIC, SST, and SLP as input variables. Note that the SIT modes are obtained by projecting the SIT data onto these eigenfunctions and performing an SVD of the projected SIT data. This is analogous to our method for finding modes for the other variables. SIT was not included in the kernel, as we found that it dominated the kernel values over other variables. Coupled NLSA produces modes in three distinct "flavors": 1) periodic modes, which reflect the seasonal cycle; 2) low-frequency modes that capture the interannual-to-decadal variability of the system; and 3) intermittent modes, which represent the interaction of low-frequency and periodic variability, in both time and space. These intermittent modes are crucial to the present study, as they encode the seasonal characteristics of sea ice reemergence. The periodic and intermittent modes come in degenerate pairs (same singular value) and evolve in temporal quadrature.

Computing the coupled NLSA kernel values and spatiotemporal modes requires choices of the Gaussian locality parameter $\epsilon$ and the spectral truncation level $l$. We use values of $\epsilon = 0.8$ and $l = 21$, $\epsilon = 1$ and $l = 23$, and $\epsilon = 1$ and $l = 24$ for the control, SOM, and CORE-II runs, respectively. The $\epsilon$ parameter is chosen empirically using the guiding principle that the coupled NLSA kernel should be as local as possible, while retaining

time-scale separation in the Laplacian eigenfunctions. In particular, when $\epsilon$ is too small, the Laplacian matrix becomes ill conditioned and the eigenfunctions become noisy and mix time scales. The truncation level $l$ is also determined empirically. In this work, $l$ was chosen in order to retain two low-frequency modes and to retain the mode pair structure of the periodic and intermittent modes.

We employ the methodology of Bushuk et al. (2015) to construct "reemergence families" of NLSA modes, which are the minimal subset of SIC modes able to reproduce the lagged correlation structure of the raw SIC data. For each model in this study, we identify a five-mode reemergence family consisting of a low-frequency mode and degenerate pairs of annual and semiannual intermittent modes. Lagged correlations computed using this family display both a melt-to-growth and a growth-to-melt reemergence of correlation. We identify associated SST, SLP, and SIT modes based on correlations with the SIC temporal modes that make up the reemergence family. This joint set of SIC, SST, SLP, and SIT modes is referred to as the reemergence family.

## 3. Growth-to-melt reemergence

Earlier work has studied low-dimensional representations of Arctic melt-to-growth reemergence and the associated physical mechanisms involving SST and SLP (Bushuk et al. 2015; Bushuk and Giannakis 2015). In this study, we use a low-dimensional description of reemergence obtained via coupled NLSA to examine Arctic growth-to-melt reemergence of SIC anomalies.

### a. Lagged correlation analysis

Sea ice reemergence is a lagged correlation phenomenon, which has been characterized via time-lagged correlation of pan-Arctic sea ice extent and area (Blanchard-Wrigglesworth et al. 2011a; Day et al. 2014b) and via time-lagged pattern correlation of Arctic SIC (Bushuk et al. 2014, 2015; Bushuk and Giannakis 2015). Here, we use the pattern correlation approach, computing time-lagged pattern correlations of the raw SIC anomaly field for all initial months (January–December) and for all lags from 0 to 23 months. Specifically, we compute an uncentered pattern correlation value for all (initial month, initial month plus lag) pairs in the time series. We report the time mean of these pattern correlations in Fig. 1. This figure shows correlations computed over a pan-Arctic domain (45°–90°N and 0°–360°) using both NSIDC observations and the CCSM4 control run. The observations (Fig. 1a) show both a melt-to-growth reemergence, corresponding to melt-season SIC anomalies recurring the following
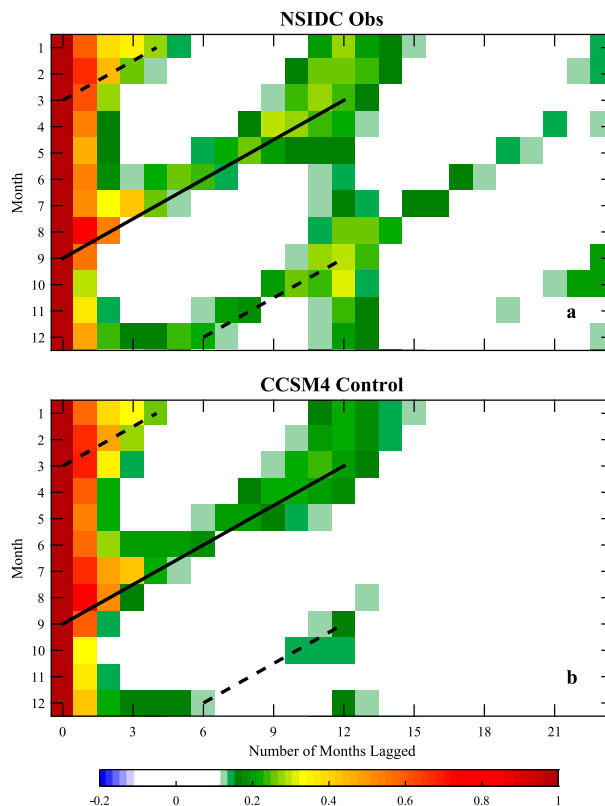


FIG. 1. Time-lagged pattern correlations of SIC anomalies from (a) NSIDC observations and (b) the CCSM4 control run, computed over a pan-Arctic domain. The solid lines indicate months with increased correlation due to melt-to-growth reemergence. The dashed lines indicate months with increased correlation due to growth-to-melt reemergence.

growth season, and a growth-to-melt reemergence, corresponding to growth-season SIC anomalies recurring the following melt season. The melt-to-growth reemergence is centered around September, with anomalies from $n$ months before September tending to reemerge $n$ months after September when the ice edge is collocated with the initial anomaly (see solid line in Fig. 1a). Similarly, the growth-to-melt reemergence is centered around March, with anomalies $n$ months before March tending to reemerge $n$ months after March (see dashed lines in Fig. 1a). The lagged correlations also show increased correlation at 12-month lag, when the ice edge is collocated with the initial anomaly. Both forms of reemergence may contribute to this correlation feature. For example, July anomalies tend to reemerge in November owing to melt-to-growth reemergence, and November anomalies tend to reemerge the following July owing to growth-to-melt reemergence. This contributes to a positive correlation at 12-month lag. It is important to note that the growth-to-melt reemergence limb strength is dependent on the observational dataset
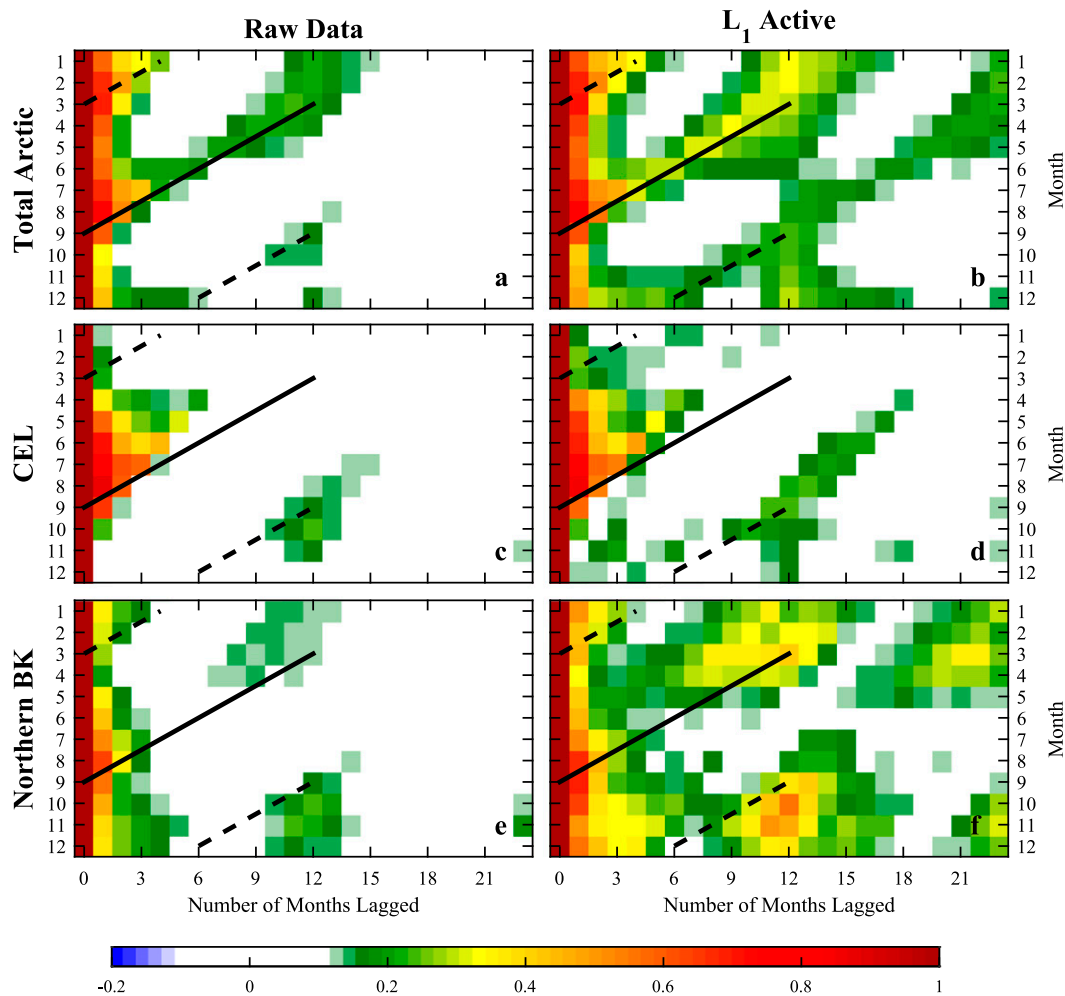
FIG. 2. Time-lagged pattern correlations of SIC anomalies from the CCSM4 control run, computed over (a),(b) a pan-Arctic domain; (c),(d) the CEL Seas; and (e),(f) the NBK Seas. Correlations are computed using the raw SIC data (left) and conditional correlations are computed over all times in which $|L_1^{SIC}| > 2$ (right). All correlations are significant at the 95% level, based on a Student's $t$ test. The solid lines indicate months with increased correlation due to melt-to-growth reemergence. The dashed lines indicate months with increased correlation due to growth-to-melt reemergence.

used. In particular, lagged pattern correlations computed using the Met Office Hadley Centre Sea Ice and Sea Surface Temperature dataset (HadISST) do not show a clear growth-to-melt limb but do display this limb during certain time periods of the record [see Figs. 12b,f of Bushuk et al. (2015)].

The CCSM4 lagged correlations (Fig. 1b) show a clear melt-to-growth reemergence, which qualitatively matches the NSIDC melt-to-growth reemergence signal, and a relatively weak growth-to-melt reemergence. In CCSM4, there is a strong temporal variability to the strength of reemergence events: during certain time periods the melt-to-growth and growth-to-melt reemergence signals are substantially enhanced. We examine this effect through additional pattern correlation analysis of CCSM4.

Specifically, this enhancement occurs when the low-frequency mode of the reemergence family, which we denote by $L_1^{SIC}$, is active. The term $L_1^{SIC}$ is the time series corresponding to the leading low-frequency SIC mode obtained via coupled NLSA. We consider this mode to be "active" when $|L_1^{SIC}| > 2$ (this corresponds to $|L_1^{SIC}| > 1.9\sigma$, where $\sigma$ is the standard deviation). Figure 2 shows correlations for pan-Arctic and regional domains computed using the raw SIC data, as well as the corresponding conditional correlations computed during times in which $L_1^{SIC}$ is active. Figures 2a and 2b show correlations computed over the pan-Arctic domain, which display a clear enhancement of both reemergence limbs when the low-frequency mode is active. The strength of the conditional growth-to-melt reemergence signal (dashed line in
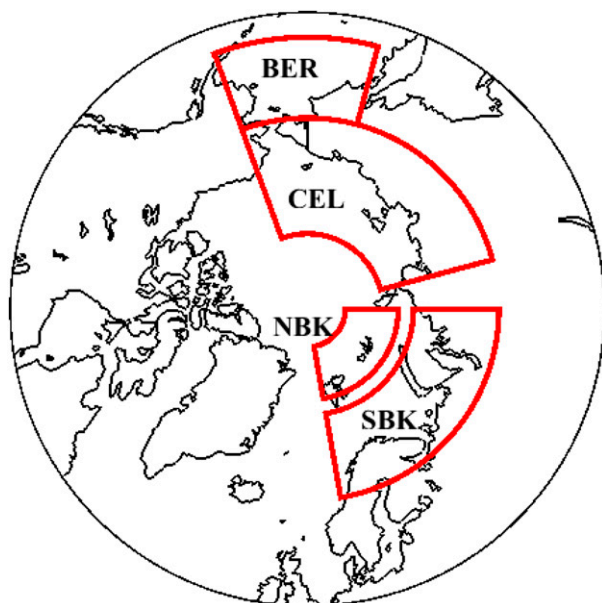
FIG. 3. Regional domains considered in this study: the CEL Seas, the NBK Seas, the Bering (BER) Sea, and the southern Barents and Kara (SBK) Seas.

Fig. 2b) is comparable to the melt-to-growth reemergence signal of the raw data (solid line in Fig. 2a).

The growth-to-melt reemergence predominantly occurs in regions of the central Arctic that are fully sea ice covered, and hence sea ice anomaly free, during the winter months. In Figs. 2c–f we compute time-lagged pattern correlations for two regions of the central Arctic: the Chukchi, East Siberian, and Laptev (CEL) Seas and the northern Barents and Kara (NBK) Seas. These regions will be focused on throughout this study. We define the CEL domain as 65°–80°N and 105°E–160°W and define the NBK domain as 78°–85°N and 10°–90°E (see Fig. 3). In each of these regions, we find that the growth-to-melt reemergence is stronger than the melt-to-growth reemergence in both the raw data and the conditional correlations. This is distinct from the pan-Arctic domain, in which melt-to-growth reemergence is decidedly stronger than growth-to-melt reemergence. The emphasized growth-to-melt reemergence in the CEL and NBK domains motivates us to focus on them in this study. Note that selecting other regions in the seasonal-ice zones would alternatively emphasize the melt-to-growth reemergence signal (Bushuk et al. 2014).

### b. SIT–SIC reemergence mechanism

We next examine the spatiotemporal evolution of the NLSA reemergence family for the CCSM4 control run, with particular focus on the role of SIT in growth-to-melt reemergence. Figure 4 shows reconstructed SIC

and SIT fields from the reemergence family for different months of the year. These are composite patterns, obtained by averaging over all times in which the low-frequency SIC mode of the reemergence family is active, in positive phase ($L_1^{SIC} > 2$). The yearly evolution and interplay of these fields reveals an SIT–SIC growth-to-melt reemergence mechanism, in which the memory of growth-season SIC anomalies is retained by SIT anomalies in the central Arctic over the winter months.

In September, we observe negative SIC anomalies in the CEL Seas and positive SIC anomalies in the NBK and Greenland Seas. Roughly spatially coincident with these anomalies are like-signed SIT anomalies. After reaching its minimum extent in September, the sea ice cover enters the growth season, characterized by southward migration of the sea ice edge and increasing SIC in the central Arctic. The SIC anomalies tend to move with the sea ice edge, eventually vacating the CEL and NBK domains, whereas the SIT anomalies are spatially persistent and insensitive to the sea ice edge position. By March, the growth-season SIC anomalies of the CEL and NBK Seas have been lost, as these seas are fully ice covered, and hence SIC anomaly free, during winter. Conversely, the SIT anomalies have persisted, retaining anomalies that are spatially coincident with the original September anomalies. The melt season begins in April, and during this season the SIC anomalies begin to retreat northward, vacating the Bering Sea and the southern portion of the Barents Sea. Eventually, the SIC anomalies move far enough northward that they begin to interact with the SIT anomalies that have been retained from the previous growth season. In the CEL domain, the ice is anomalously thin and melts out faster than normal, creating a negative SIC anomaly in this region. Conversely, the NBK Seas have anomalously thick ice, meaning that the ice melts out more slowly than normal, creating a positive SIC anomaly. By this mechanism, growth-season SIC anomalies tend to reemerge the following melt season. After reemerging, the anomalies are maintained up to the September sea ice minimum. This cycle roughly repeats again the following year, and, as we find in the following subsection, these "reemergence events" tend to recur over 3–10-yr time periods.

Sea ice reemergence requires both a source of variability, which sets up the initial SIC anomaly pattern, and a source of memory, which acts to retain the anomaly between the growth and melt seasons. In the SIT–SIC mechanism above, persistent SIT anomalies act as the source of memory, but this does not preclude an oceanic or atmospheric role in driving the patterns of SIT–SIC covariability shown in Fig. 4. In particular, earlier work has shown that large-scale modes of SLP
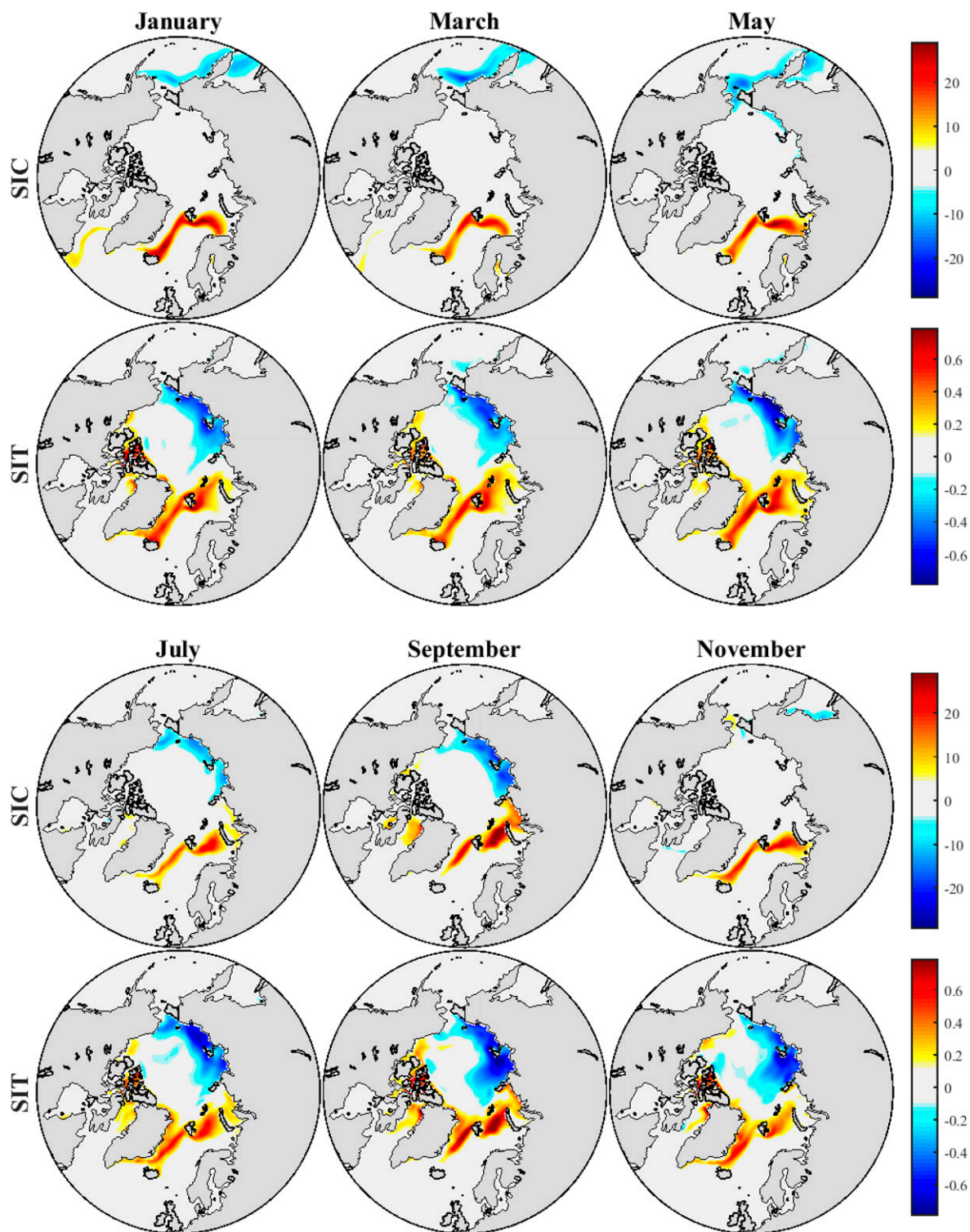
FIG. 4. Spatial pattern composites of SIC (%) and SIT (m), computed using the NLSA reemergence family of the control run. These composites are computed over all times in which the leading low-frequency SIC mode is active in positive phase ($L_1^{SIC} > 2$).

variability provide a dynamical linkage, which sets the spatial patterns of SIC reemergence (Bushuk and Giannakis 2015). In Fig. 5, we consider oceanic and atmospheric contributions to reemergence, plotting the reconstructed SST and SLP fields from the control run reemergence family. The SLP patterns of the reemergence family closely resemble the Arctic dipole anomaly pattern of SLP variability (Wu et al. 2006). The SLP modes from coupled NLSA capture low-frequency atmospheric regimes and represent a temporally low-pass-filtered version of the atmospheric state [see Fig. 8 of Bushuk et al. (2015)]. By virtue of filtering out high frequencies, these modes have substantially more persistence than the full SLP field, which has little autocorrelation beyond one month. In their positive phase, these SLP patterns drive geostrophic winds that blow meridionally from the North Pacific sector to the North Atlantic sector. These winds influence sea ice dynamically, exporting ice from the CEL domain into the NBK domain, and thermodynamically, via the advection of warm air into the CEL domain and cold air into the NBK domain. These factors contribute to anomalous melting and export in the CEL domain and anomalous freezing and import in the NBK domain, consistent with the ice anomalies in Fig. 4. This suggests that the dipole anomaly SLP pattern plays a role in setting the spatial pattern of sea ice reemergence in two related ways: 1) driving SIC anomalies near the ice edge and 2) driving SIT anomalies in the central Arctic. The SLP anomalies are strongest in the ice growth season of October–March, encoding the spatial pattern of future melt-season anomalies. While atmospheric variability provides an important control on SIC and SIT variability, the atmosphere cannot provide a stand-alone reemergence mechanism because of its low autocorrelation on time scales beyond one month. Rather, the atmosphere sets up initial SIT and SIC anomalies, and this signal is persisted via central Arctic SIT anomalies. This SIT memory allows for reemergence of SIC between the growth season and the melt season.

Aside from anomalies adjacent to the summer sea ice edge, there is no clear SST signal in the central Arctic owing to the fact that these grid points are primarily covered by sea ice. This indicates that mixed layer ocean temperatures in the central Arctic do not provide a source of memory for growth-to-melt reemergence. We will return to the role of the ocean in growth-to-melt reemergence in section 5, when we investigate sea ice reemergence in a model hierarchy.

### c. Metrics for growth-to-melt reemergence

Next, we introduce a set of reemergence metrics, by which one can judge the amplitude and phase of

reemergence events, and assess the activity of the SIT–SIC reemergence mechanism. These metrics shed light on the temporal behavior of sea ice reemergence. We define SIC and SIT metrics as the integrated SIC and SIT anomalies, respectively, over a region of interest. These metrics, computed over the CEL and NBK domains using the control run reemergence family, are shown in Fig. 6. Note that the metrics have been normalized by their standard deviation.

Growth-to-melt reemergence events can be identified as periods of time during which the SIC reemergence metrics (Fig. 6a) have large amplitude and consistent sign over a number of consecutive years. The SIC metrics pulse with an annual cycle, with large amplitude in summer months and small amplitude in winter months. These metrics also display a clear antiphase relationship between the SIC anomalies of the CEL and NBK domains. The SIT reemergence metrics (Fig. 6b) have the same sign as the SIC metrics but do not display an annual pulsing. Rather, the SIT metrics persist with the same sign for a number of years and closely resemble modulating envelopes for the SIC metrics. This relationship reflects the SIT–SIC reemergence mechanism described above, with SIT retaining memory that allows SIC anomalies to reemerge in successive summers. Figures 6c and 6d display a zoom-in of these metric values for a 4-yr period of active reemergence. We observe that the SIC metric is small over the winter months and large over summer months. The SIT metric maintains a persistent sign over this 4-yr time period, matching the sign of the SIC anomalies.

It is important to note that the SIC metrics show more than simply the seasonal cycle in SIC variability in these regions. The amplitude of the SIC metrics have a seasonal cycle, as the CEL and NBK domains have low SIC variability in the ice-covered winter months and high variability in the summer months (see Fig. 8a, described in greater detail below). The crucial point shown in Fig. 6 is that the SIC metrics tend to have a repeated sign in successive years, indicating a reemergence of SIC anomalies.

## 4. Seasonality and interannual variability of sea ice reemergence mechanisms

The control run reemergence family captures both growth-to-melt as well as melt-to-growth reemergence of SIC anomalies (see Fig. 2b). In the previous section, we have demonstrated that the family displays an SIT–SIC mechanism for growth-to-melt reemergence. Additionally, the SST and SLP patterns of this family reflect the SST–SIC and SLP–SIC mechanisms for melt-to-growth reemergence presented in earlier work (see Figs. 4 and 5; Bushuk and Giannakis 2015). This motivates a simultaneous
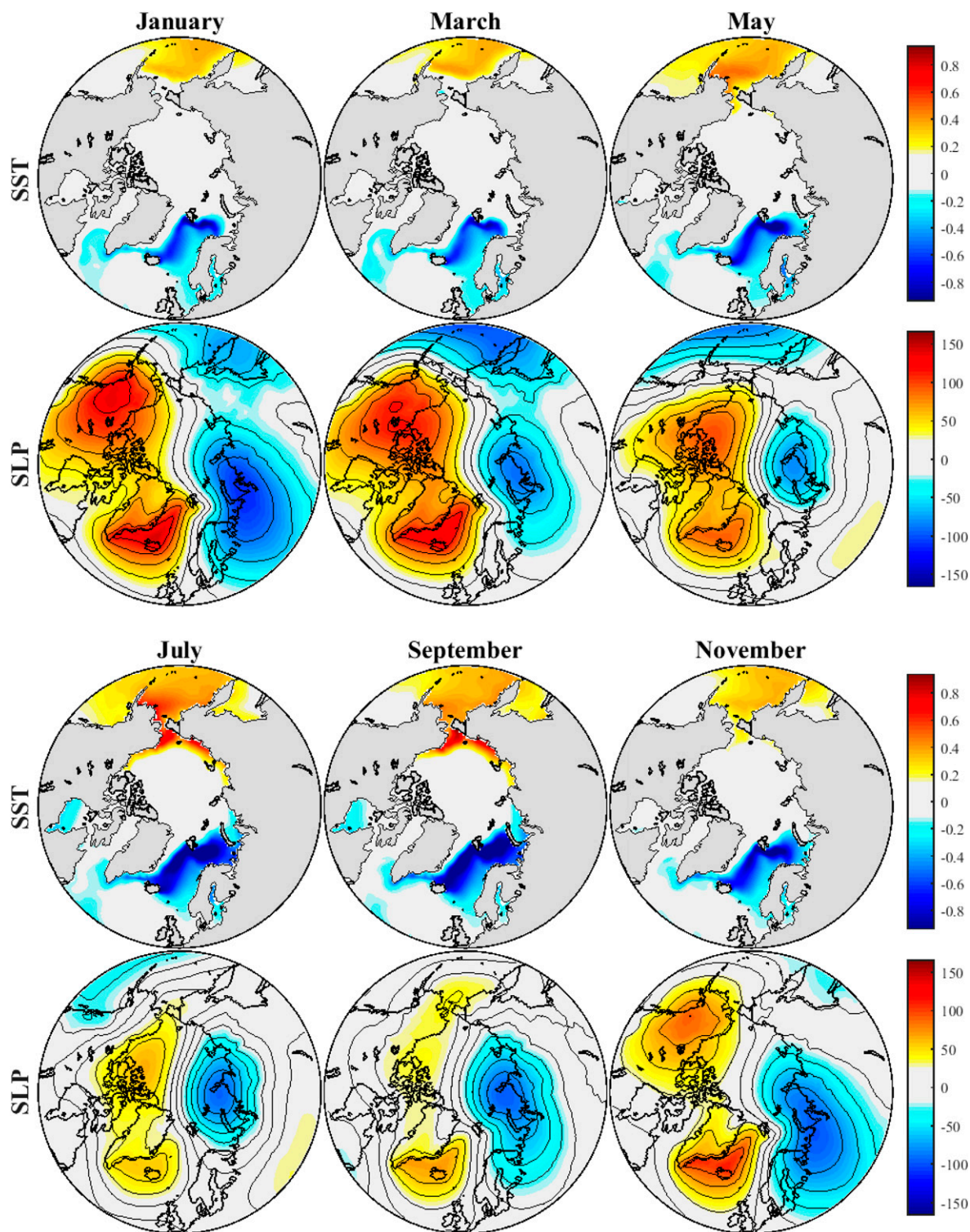
FIG. 5. Spatial pattern composites of SST (K) and SLP (Pa), computed using the NLSA reemergence family of the control run. SLP contours are plotted in black. These composites are computed over all times in which the leading low-frequency SIC mode is active in positive phase ($L_1^{SIC} > 2$).
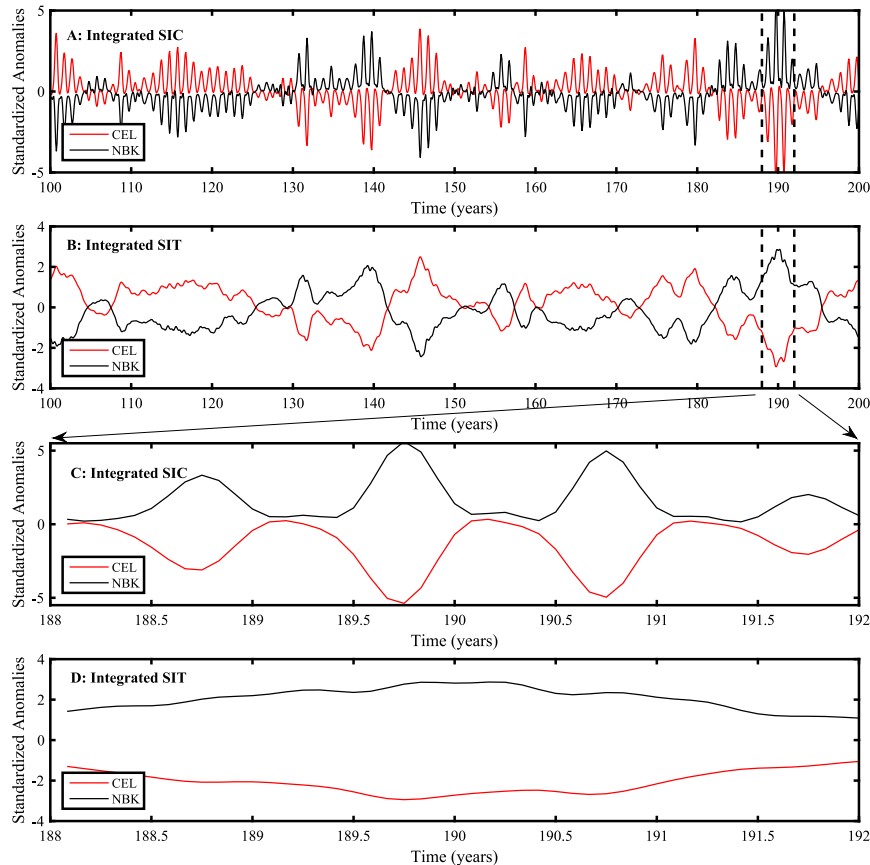
FIG. 6. SIC and SIT reemergence metrics computed using the control run NLSA re-emergence family for the CEL and NBK domains. The metrics are normalized by their std dev. (a),(b) A 100-yr portion of the time series; (c),(d) a 4-yr portion.

comparison of all four fields of the reemergence family. In Fig. 7, we investigate the seasonality and phase relationships of these three reemergence mechanisms. We find that each reemergence mechanism displays a clear relation to the seasonal cycle, involving interaction between SIC anomalies and a second physical variable of the ice–ocean–atmosphere system.

Figure 7 (left) shows reemergence metrics plotted for a 4-yr time period of active reemergence (the same 4-yr period as used in Fig. 6). In all panels, SIC metrics are plotted as solid lines, and the metrics for the field that participates in the reemergence mechanism are plotted as dashed lines. Figures 7 (center and right) show the phase evolution of these metrics with respect to the seasonal cycle. Specifically, for each metric $M(t)$, the phase evolution is given by $(x[t], y[t]) = (|M[t]|\cos[2\pi t/12], |M[t]|\sin[2\pi t/12])$, where parentheses are used to indicate coordinate pairs and where $t$ is the time measured in months. We plot these values for an 80-yr portion of the time series. The phase plots are qualitatively similar for other 80-yr portions of the 1300-yr time series. As stated in

section 3c, the SIC and SIT metrics are defined as the integrated SIC and SIT anomalies over a region of interest. Following Bushuk et al. (2015), the SST metric is defined as the integrated SST anomaly computed over the region that experiences summer imprinting of SST anomalies and the SLP metric as the mean value of the meridional geostrophic wind computed over the region of interest. Figures 7a–c each focus on a particular reemergence mechanism. The time series and phase diagrams should be considered in concert. In particular, the phase diagrams illustrate the seasonality and interannual variability of the reemergence mechanism (but do not contain information about the sign of the metrics), whereas the time series illustrate the metrics and their sign during a particular 4-yr period of active reemergence. Taken together, these plots describe the temporal behavior of these mechanisms over an 80-yr time period.

Figure 7a shows the SIT and SIC metrics computed for the CEL and NBK domains. The 4-yr snapshot is that of Figs. 6c and 6d, illustrating the SIT–SIC reemergence mechanism with persistent SIT anomalies providing the
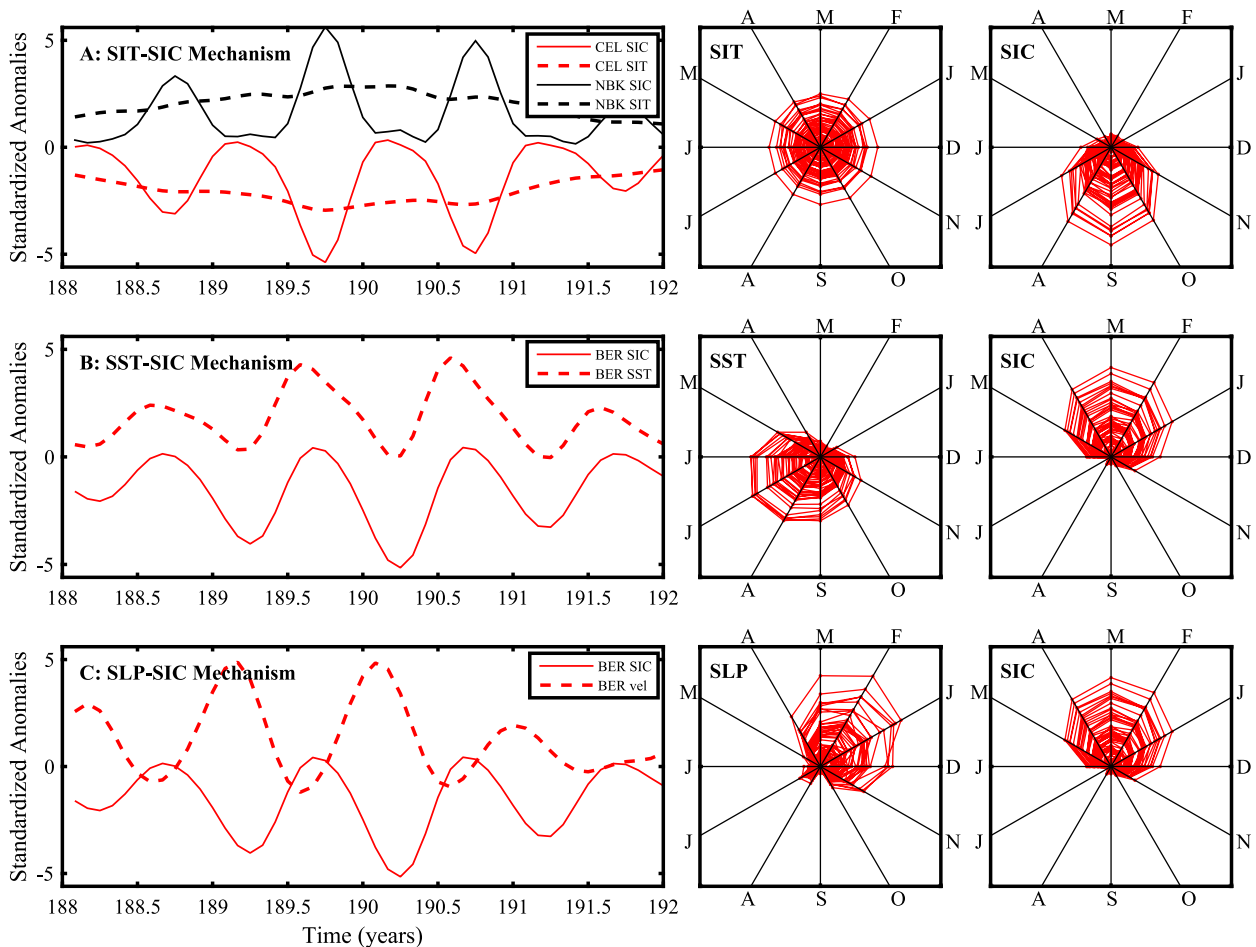
FIG. 7. Time series and phase evolution of reemergence metrics for SIC, SST, SLP, and SIT, computed using the control run NLSA reemergence family over the CEL, NBK, and BER domains. Each row highlights an individual reemergence mechanism: (a) the SIT–SIC mechanism for growth-to-melt reemergence, (b) the SST–SIC mechanism for melt-to-growth reemergence, and (c) the SLP–SIC mechanism for melt-to-growth reemergence. (left) Time series during a 4-yr period of active reemergence, with SIC metrics plotted as solid lines and metrics for the other variables participating in the mechanism plotted as dashed lines. (center),(right) The seasonal phase evolution of the absolute values of the metrics, plotted for an 80-yr portion of the time series.

memory for growth-season SIC anomalies to reemerge the following melt season. The phase evolution of these metrics clearly illustrates the persistence of the SIT anomalies and the seasonality of the SIC anomalies. The SIT metric tends to be active during all months of the year, with relatively circular trajectories in phase space, whereas the SIC metric tends to be strongly active in summer, peaking in September, and weakly active during the winter months. The radial variations in these phase plots illustrate the substantial interannual variability in the magnitude of reemergence events.

In Fig. 7b, we plot SST and SIC metric values for the Bering Sea, a region with particularly strong melt-to-growth reemergence in this model (see Figs. 4 and 5). The Bering SIC metrics are computed over 55°–65°N and 165°E–160°W and the Bering SST metrics are

computed over 60°–65°N and 165°E–160°W. For visual clarity we do not plot metrics from the southern Barents and Kara Seas, which display similar qualitative behavior and are out of phase with the Bering Sea metrics. The 4-yr snapshot shows that the SIC metric is large in winter and small in summer. The SST metric has opposite sign to the SIC metric and is large in summer and small in winter. These metrics illustrate a trade-off between SST and SIC, in which summer SST anomalies store the memory of winter SIC anomalies. This SST memory allows for SIC anomalies to reemerge the following growth season, as displayed by the metrics. The phase evolution clearly demonstrates this SST–SIC trade-off, as the SIC metric is strongly active in winter months and the SST metric is strongly active in summer months. Indeed, the sum of these two phase portraits
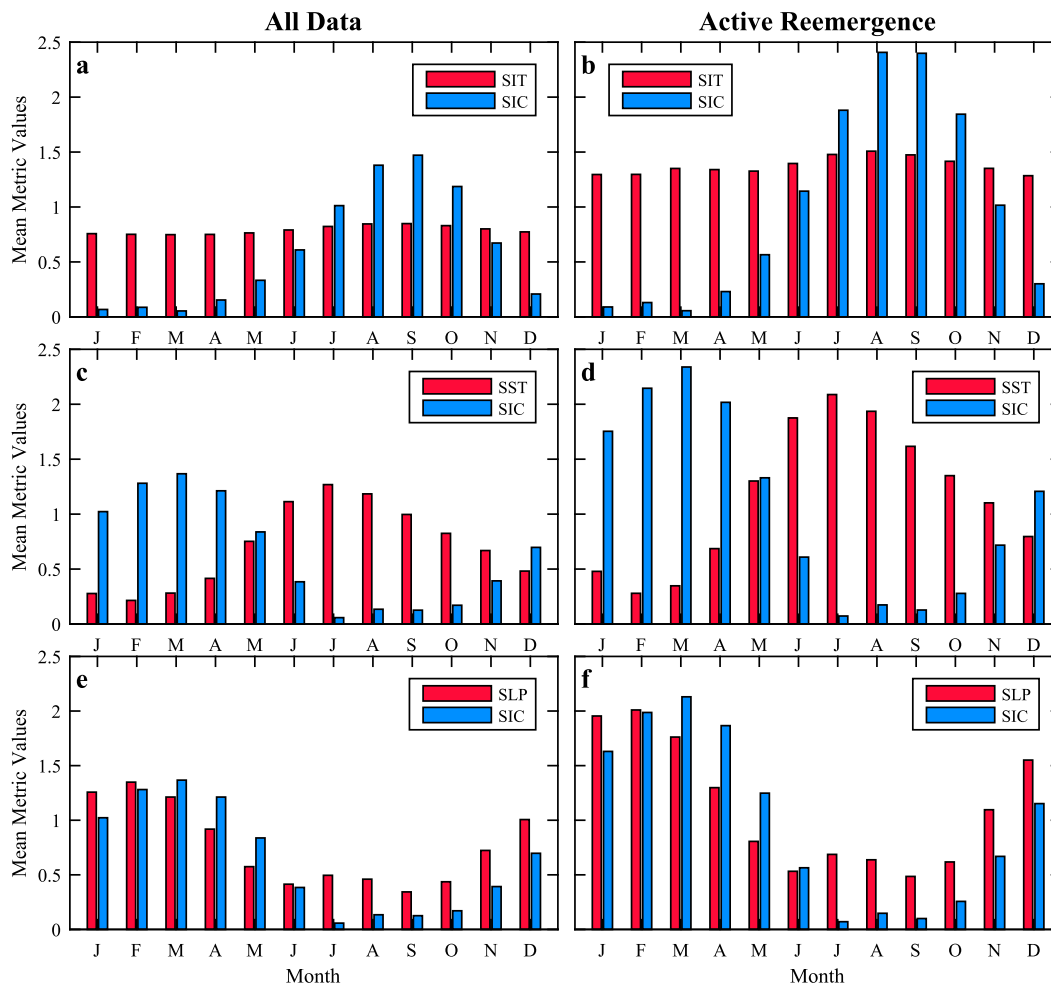
FIG. 8. Time-mean amplitude of reemergence metrics for SIC, SST, SLP, and SIT, for different months of the year, computed using the full time series and during periods of active reemergence. These metrics are computed using the NLSA reemergence family, over the same domains as Fig. 7.

would yield a result with relatively circular trajectories in phase space.

Finally, in Fig. 7c, we plot SLP and SIC metrics for the Bering Sea. Again, the southern Barents–Kara metrics display similar behavior, which we choose not to plot for visual clarity. The meridional winds have opposite sign to the SIC anomalies and have largest amplitude during the winter months. This anticorrelation suggests a physical SLP–SIC interaction, as positive (i.e., warm) meridional winds correspond to negative SIC anomalies, and vice versa. The physical consistency of the SIC and SLP fields, along with the winter-to-winter persistence of the SLP patterns, provides an SLP–SIC mechanism for reemergence. Note that earlier work has shown that SST provides the dominant source of memory for melt-to-growth reemergence and that the SLP mechanism does not operate as a stand-alone process (Bushuk et al. 2015). The SLP mechanism plays a key role,

however, in setting the spatial patterns of melt-to-growth SIC reemergence. The phase diagrams illustrate that the wind anomalies generally lead the SIC anomalies, as the winds are maximal in January and February, whereas the SIC anomalies peak in March. This relationship, with wind anomalies leading and SIC anomalies lagging, is consistent with the physical expectation that these SIC anomalies are forced by atmospheric circulation anomalies. Additional work, investigating the causality of this SLP–SIC lead–lag relationship, is required.

Note that the same time period is used for the three mechanisms shown in Fig. 7. This indicates that, for the NLSA reemergence family, periods of active melt-to-growth reemergence coincide with periods of active growth-to-melt reemergence. This tendency is also displayed by the raw data, as certain time periods are characterized by both enhanced melt-to-growth and growth-to-melt reemergence (see Figs. 2a,b).

Next, building on Fig. 7, we consider the interannual variability of the three sea ice reemergence mechanisms. Figure 8 (left) shows the mean absolute value of each reemergence metric for each month of the year. These metrics are computed over the same domains as Fig. 8 (the SIT metric values are shown for the CEL domain). Figures 8a, 8c, and 8e show the same seasonal relationships discussed above: persistent SIT anomalies with SIC anomalies that peak in September and decay to zero over the winter months (Fig. 8a), summer SST anomalies that trade-off with winter SIC anomalies (Fig. 8c), and SLP anomalies that lead winter SIC anomalies by roughly 1 month (Fig. 8e). We next compute analogous quantities for time periods of active reemergence. Specifically, we compute the mean absolute value of each reemergence metric, conditional on times in which $|L_1^{SIC}| > 2$. These conditional means are plotted in Figs. 8b, 8d, and 8f. The periods of active reemergence display a similar seasonality to the time mean, but the strength of each reemergence mechanism is significantly enhanced during these time periods. The enhancement is clear both in the SIC metrics and in the second variable that participates in the reemergence mechanism. The anomaly magnitudes increase by nearly a factor of 2 for all variables during these periods of active reemergence. This fact may have implications for seasonal to interannual predictability of Arctic sea ice since any reemergence-based predictability will be enhanced during these active periods and reduced during inactive periods.

## 5. Investigation using a model hierarchy

We now further explore the results presented above by examining sea ice reemergence in a CCSM4 hierarchy. The model hierarchy, as described in section 2, consists of the fully coupled control run, a mixed layer ocean model (the SOM run), and an ice–ocean model forced by CORE-II surface fields (the CORE-II run). The growth-to-melt reemergence is similar in all three models, whereas the control and CORE-II runs have a stronger melt-to-growth reemergence than the SOM [see Fig. 3 of Bushuk and Giannakis (2015)]. The representation of melt-to-growth reemergence in this hierarchy has been explored in earlier work (Bushuk and Giannakis 2015), so we focus our attention here on growth-to-melt reemergence and the seasonality of reemergence mechanisms across the models.

### a. Growth-to-melt reemergence

Figure 9 shows reconstructed summer (July–September) patterns of SIC and SIT, computed using the reemergence-mode families of each model. These patterns are composites, computed over all times in which $L_1^{SIC}$ of

each reemergence family is active, in positive phase. The thresholds used to define active are $|L_1^{SIC}| > 2$ for the control run and $|L_1^{SIC}| > 1.5$ for the shorter SOM and CORE-II runs. We find that the summer patterns of SIC and SIT are similar between the control and the SOM, both in terms of spatial distribution and anomaly magnitude. In both models, the summer SIT anomalies extend farther northward than the SIC anomalies, indicating the presence of anomalous SIT in the perennially ice-covered regions of the central Arctic. The similarity of the SOM and the control suggests that the dynamics represented by a full-depth ocean model are not critical in accurately capturing summer SIT–SIC covariability. This is consistent with the expectation that vertical mixing in the strongly stratified Arctic upper ocean should not play a leading-order role in driving summer sea ice variability. This similarity suggests that SOM-based seasonal forecasts of summer sea ice could offer a computationally efficient alternative to fully coupled dynamical forecast systems.

The CORE-II run has very different patterns of summer SIC and SIT variability than the control, characterized by SIC anomalies spanning most of the central Arctic, and an SIT pattern dominated by anomalies north of the Canadian Archipelago and Greenland. These anomalies lack the dipole structure of the control and SOM runs. Earlier work has suggested that this difference results from the lack of ocean-to-atmosphere coupling in the CORE-II run (Bushuk and Giannakis 2015). This difference may also be related to the relatively short (60 yr) reanalysis-based dataset that is used to force this simulation. The SIT–SIC covariability is also degraded in this model: the pattern correlation between the SIT and SIC fields in Fig. 9 is 0.62 for the CORE-II run, compared with 0.84 for the control and 0.75 for the SOM. We also find that the magnitude of the CORE-II SIT anomalies is substantially smaller than the other models, which is likely related to the model's thin bias (Blanchard-Wrigglesworth and Bitz 2014). This thin bias also contributes to the presence of SIC anomalies at central Arctic grid points that are perennially ice covered in the control and SOM runs. These SIT and SIC patterns demonstrate that forced ice–ocean models can exhibit vastly different patterns of SIT–SIC covariability than their fully coupled counterparts.

### b. Seasonality of reemergence

Next, using the SOM and CORE-II reemergence mode families, we compute reemergence metrics and study their seasonal evolution. Figures 10 and 11 are analogs to Fig. 7, showing reemergence metrics for 4-yr periods of active reemergence and the phase evolution of these metrics, for the SOM and CORE-II runs,
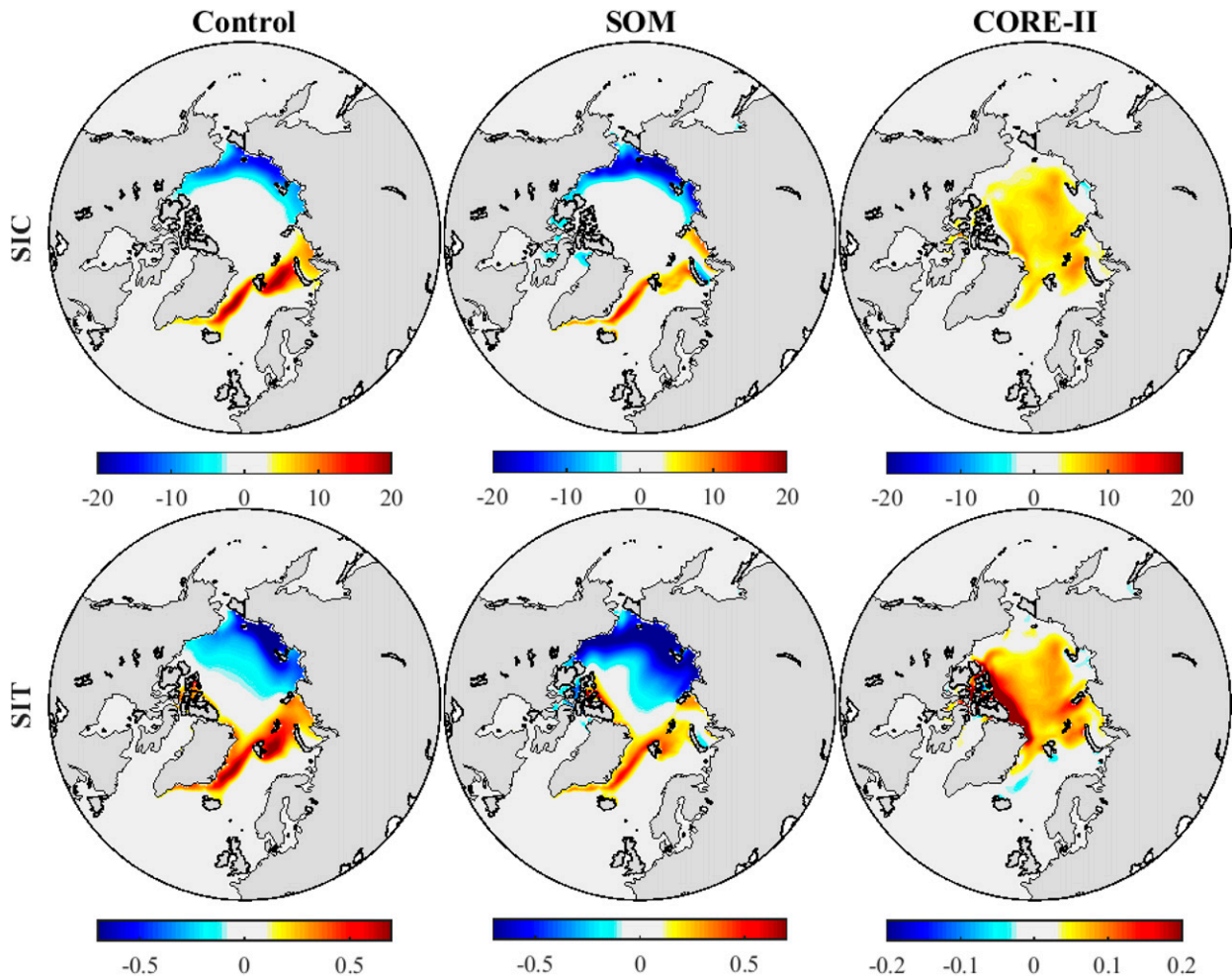
FIG. 9. Summer (JAS) composites for (top) SIC (%) and (bottom) SIT (m) computed using the reemergence mode families of the (left) control run, (middle) SOM run, and (right) CORE-II run. The composites are computed over all times in which $L_1^{SIC}$ of each family is active, in positive phase. Note that a different color bar is used for SIT in the CORE-II run.

respectively. The SOM displays a clear SIT–SIC growth-to-melt reemergence mechanism, which closely resembles that of the control run. The seasonal phase evolution is also similar to the control run, characterized by persistent central Arctic SIT anomalies and SIC anomalies that are large in the summer and small in the winter. The SOM also displays the SST–SIC and SLP–SIC melt-to-growth reemergence mechanisms. Each of these mechanisms has similar seasonal relationships to those observed in the control run. In particular, the SOM summer SST anomalies trade off with winter SIC anomalies and the SOM SLP anomalies tend to lead the SIC anomalies by roughly 1 month. Note that the metrics here are plotted for a Bering Sea domain; in other regions, such as the Barents Sea, the SST–SIC mechanism fidelity is degraded in the SOM (Bushuk and Giannakis 2015).

The seasonality of the CORE-II reemergence metrics display a coarse-level agreement with the control and SOM runs; however, they also display a number of notable differences. As noted earlier, the CEL and NBK SIT anomalies do not display the dipole pattern seen in the control run and the SOM. The phase evolution in Fig. 11 reveals interannually persistent SIT anomalies in these regions and SIC anomalies that are large in summer months and negligible in winter months. While the seasonality of the SIT–SIC mechanism is similar to the other models, it is important to note that the CORE-II SIT metric values tend to cluster more closely to zero, compared to the SOM and control SIT metrics, which display a more uniform foliation of phase space.

The CORE-II reemergence metrics for the SST and SLP mechanisms were computed over the southern Barents–Kara domain, since this model has very little
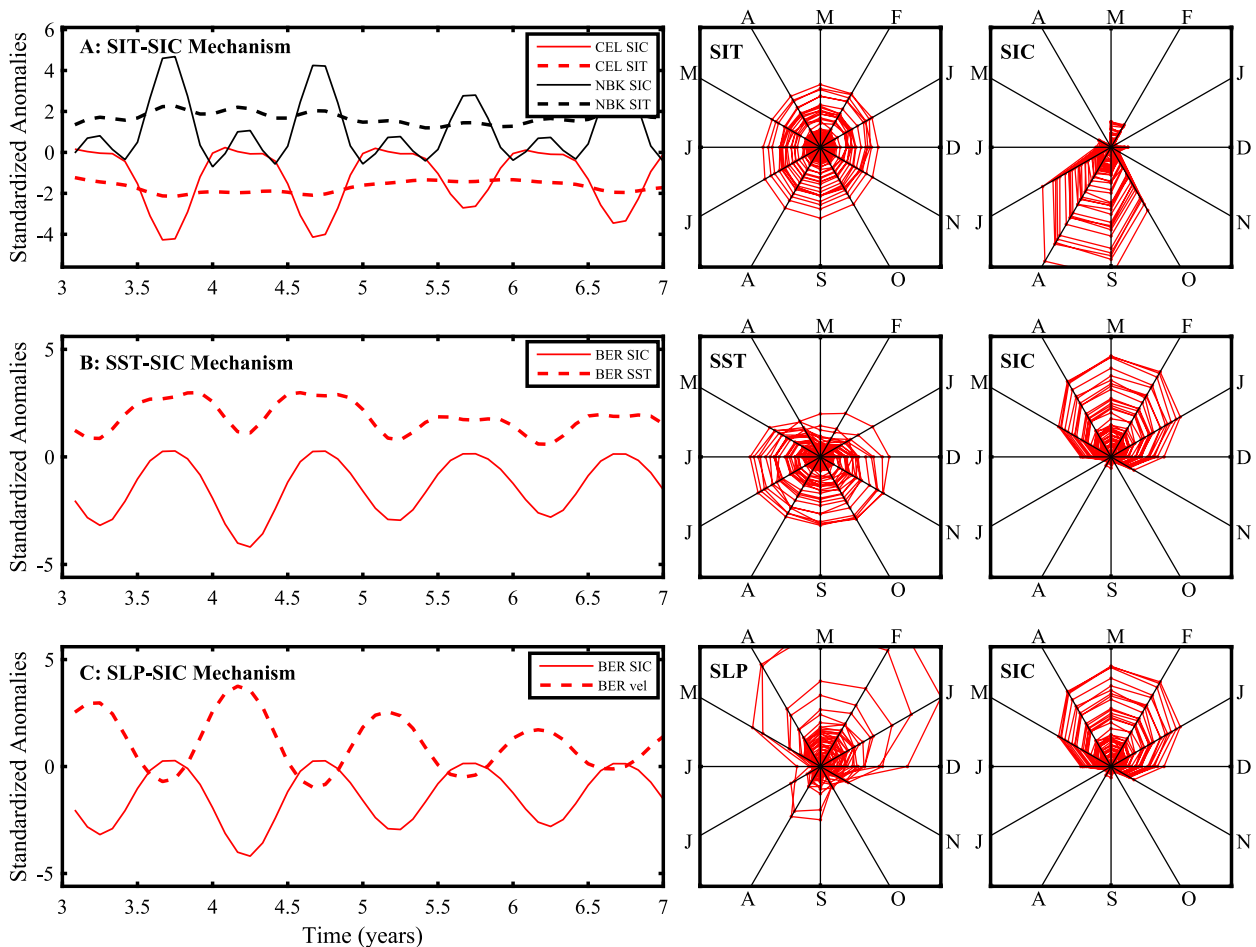
FIG. 10. Time series and phase evolution of reemergence metrics for SIC, SST, SLP, and SIT. These metrics are computed using the NLSA reemergence family from the SOM run.

winter SIC variability in the Bering Sea. Specifically, the SIC and SLP metrics are computed over the region defined by 65°–75°N and 10°–90°E, and the SST metric is computed over 65°–75°N and 60°–90°E, the region imprinted with summer SST anomalies. The CORE-II SIC and SST metrics are out-of-phase, exhibiting a trade-off between winter SIC anomalies and summer SST anomalies. Compared to the Bering SIC anomalies from the control run, the CORE-II Barents–Kara SIC anomalies occur slightly later in the season. Correspondingly, the SST anomalies in this region are also delayed by roughly one month. The relation between SLP and winter SIC is less clear in CORE-II than the other models. The CORE-II SLP metrics are noisier and also display substantial anomalies over the summer months. The CORE-II SLP anomalies lead the SIC anomalies by roughly 2–3 months, which is a substantially longer lead time than the control and SOM runs. In summary, the seasonal relationships in CORE-II

are consistent with the other models, but the detailed phase information and covariability mechanisms are generally degraded in this model.

## 6. Conclusions

In this work, we have used a hierarchy of global climate models (GCMs) in the Community Climate System Model, version 4 (CCSM4), framework to examine the seasonality and interannual variability of Arctic sea ice reemergence. We first studied the growth-to-melt-season reemergence of Arctic sea ice concentration (SIC) anomalies in a CCSM4 control integration. We employed a mode-based approach for this analysis, utilizing spatiotemporal modes of covariability to form low-dimensional representations of sea ice reemergence. These spatiotemporal modes of variability were obtained via coupled nonlinear Laplacian spectral analysis (NLSA), a data analysis technique for high-dimensional
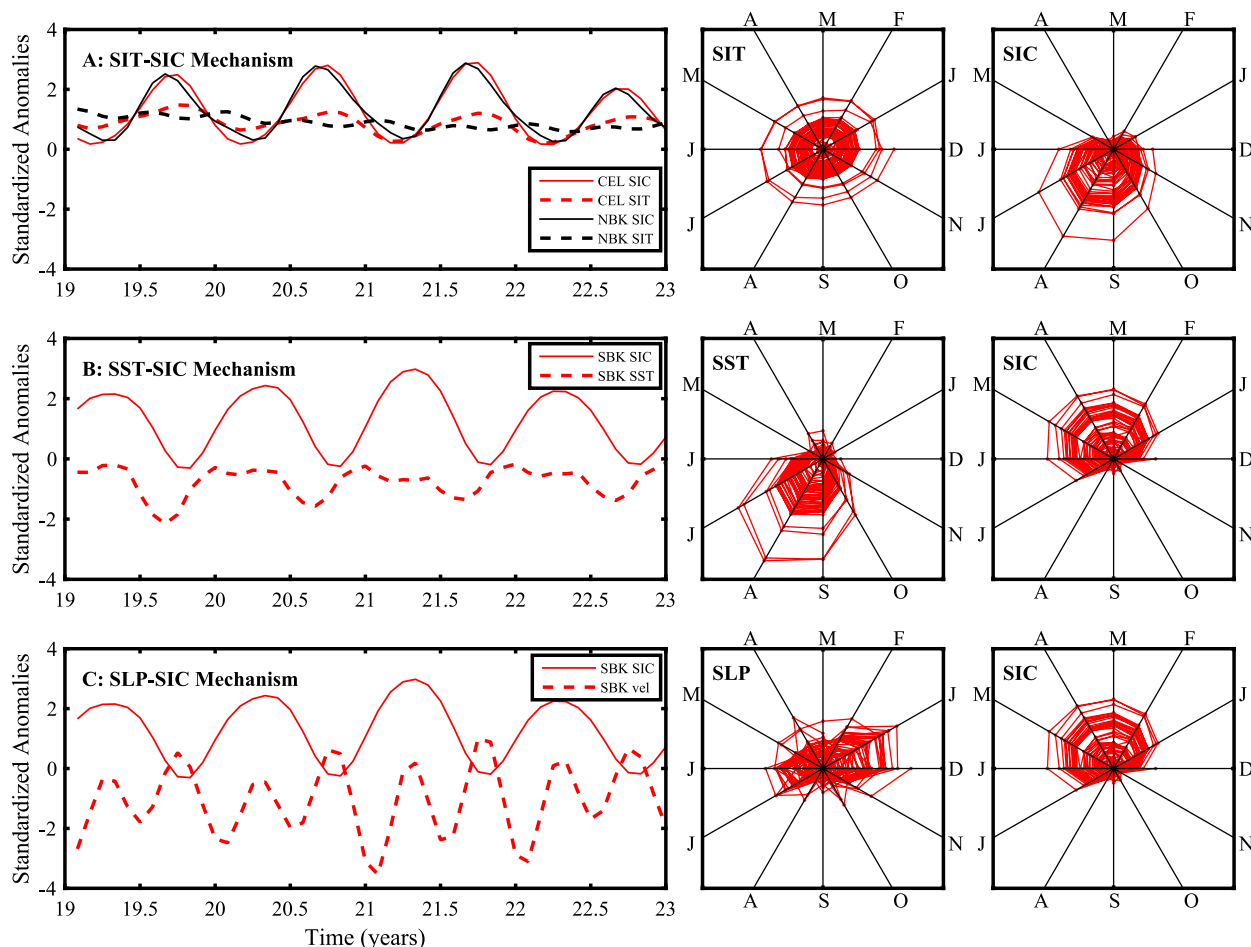
FIG. 11. Time series and phase evolution of reemergence metrics for SIC, SST, SLP, and SIT. These metrics are computed using the NLSA reemergence family from the CORE-II run.

multivariate time series. The coupled NLSA modes capture the covariability of SIC, sea surface temperature (SST), sea level pressure (SLP), and sea ice thickness (SIT). Using these modes, we constructed a five-mode reemergence family, which captures both the growth-to-melt and melt-to-growth reemergence of Arctic SIC anomalies. This reemergence family captures the spatiotemporal evolution of SIC, SST, SLP, and SIT, allowing us to simultaneously study these fields in relation to sea ice reemergence.

Time-lagged pattern correlations of raw SIC data from CCSM4 and observations from the National Snow and Ice Data Center (NSIDC) display both melt-to-growth and growth-to-melt reemergence of SIC anomalies. The growth-to-melt reemergence is most active in regions of the central Arctic, such as the Chukchi, East Siberian, and Laptev (CEL) Seas and the northern Barents and Kara (NBK) Seas. Both types of reemergence are enhanced during periods of time in which

the low-frequency mode of the reemergence family is active. The low-dimensional reemergence family captures an SIT–SIC growth-to-melt reemergence mechanism, in which growth-season SIC anomalies imprint like-signed SIT anomalies in the central Arctic (Blanchard-Wrigglesworth et al. 2011a). These SIT anomalies persist over the winter months, when the central Arctic becomes fully ice covered and loses its growth-season SIC anomalies. As ice melts the following melt season, the ice edge moves northward, interacts with the SIT anomalies, and reinherits SIC anomalies of the same sign as the previous growth season. The SLP patterns of the reemergence family resemble the Arctic dipole anomaly mode of variability, driving out-of-phase sea ice variations between the CEL and NBK domains. The SLP patterns are strongest in the ice growth season, setting SIC patterns that reemerge the subsequent melt season. While atmospheric circulation anomalies are an important driver of SIC variability, central Arctic SIT

anomalies provide the crucial source of memory for growth-to-melt reemergence.

We have introduced SIC and SIT reemergence metrics, by which one can judge the amplitude and phase of reemergence events and the SIT–SIC reemergence mechanism. These metrics display interannual-to-decadal variability in the strength, sign, and duration of reemergence events. They also clearly display the SIT–SIC mechanism described above. Consideration of SST and SLP reemergence metrics demonstrated that the reemergence family additionally captured SST- and SLP-based mechanisms for melt-to-growth sea ice reemergence. The SLP mechanism drives the spatial patterns of reemerging SIC anomalies, whereas the SST mechanism provides the key source of memory for melt-to-growth reemergence. Seasonal phase diagrams revealed that each of these mechanisms has a clear relationship to the seasonal cycle. In particular, we found that 1) the SIT–SIC mechanism is characterized by interannually persistent SIT anomalies and SIC anomalies that are large in summer and small in winter, 2) the SST–SIC mechanism displays a clear trade-off between winter SIC anomalies and summer SST anomalies, and 3) the SLP–SIC mechanism has large SIC and SLP anomalies in winter, with the SLP anomalies leading SIC by roughly one month. We have also found that each of these mechanisms exhibit clear periods of active reemergence, in which both the SIC anomalies and the related variable that participates in the reemergence mechanism are substantially enhanced. The low-frequency mode of the reemergence family is a good predictor of these periods of enhanced reemergence. These results complement the work of Bushuk and Giannakis (2015) on melt-to-growth reemergence, providing a unified description of melt-to-growth and growth-to-melt reemergence in terms of a single family of modes.

We have also examined sea ice reemergence in a model hierarchy consisting of the control run, a slab-ocean model (SOM), and an ice–ocean model forced by phase II of the Co-ordinated Ocean–Ice Reference Experiments (CORE-II) atmospheric fields. Our primary finding was that the control and SOM runs have a similar representation of sea ice reemergence across a number of key criteria, including SIT–SIC covariability; the SIT–SIC growth-to-melt reemergence mechanism; and the seasonality and interannual variability of the SIT–SIC, SST–SIC, and SLP–SIC mechanisms. On the other hand, the CORE-II run, while displaying a coarse-level agreement with the control and SOM, exhibits a degraded representation of growth-to-melt and melt-to-growth reemergence mechanisms. These results suggest that coupled ice–ocean–atmosphere models are

essential in accurately representing sea ice reemergence and its associated physical mechanisms. A priority for future work is to examine the SIT–SIC growth-to-melt reemergence mechanism using available observational data and ice–ocean reanalysis products.

This work has highlighted the seasonality and interannual variability of three physical mechanisms that underlie the memory of Arctic sea ice. These mechanisms imply that accurate initialization and simulation of SIT is crucial for seasonal predictions of summer sea ice, whereas initialization and simulation of SST and SLP is key for winter sea ice prediction. This work also suggests that coupled NLSA may be a useful approach for studying other climate phenomena that involve interaction between low-frequency variability and the seasonal cycle.

REFERENCES

Belkin, M., and P. Niyogi, 2003: Laplacian eigenmaps for dimensionality reduction and data representation. *Neural Comput.*, **15**, 1373–1396, doi:10.1162/089976603321780317.

Bitz, C., and G. Roe, 2004: A mechanism for the high rate of sea ice thinning in the Arctic Ocean. *J. Climate*, **17**, 3623–3632, doi:10.1175/1520-0442(2004)017<3623:AMFTHR>2.0.CO;2.

——, K. Shell, P. Gent, D. Bailey, G. Danabasoglu, K. Armour, M. Holland, and J. Kiehl, 2012: Climate sensitivity of the Community Climate System Model, version 4. *J. Climate*, **25**, 3053–3070, doi:10.1175/JCLI-D-11-00290.1.

Blanchard-Wrigglesworth, E., and C. M. Bitz, 2014: Characteristics of Arctic sea-ice thickness variability in GCMs. *J. Climate*, **27**, 8244–8258, doi:10.1175/JCLI-D-14-00345.1.

——, K. C. Armour, C. M. Bitz, and E. DeWeaver, 2011a: Persistence and inherent predictability of Arctic sea ice in a GCM ensemble and observations. *J. Climate*, **24**, 231–250, doi:10.1175/2010JCLI3775.1.

——, C. Bitz, and M. Holland, 2011b: Influence of initial conditions and climate forcing on predicting Arctic sea ice. *Geophys. Res. Lett.*, **38**, L18503, doi:10.1029/2011GL048807.

Broomhead, D. S., and G. P. King, 1986: Extracting qualitative dynamics from experimental data. *Physica D*, **20**, 217–236, doi:10.1016/0167-2789(86)90031-X.

Budyko, M., 1969: The effect of solar radiation variations on the climate of the earth. *Tellus*, **21**, 611–619, doi:10.3402/tellusa.v21i5.10109.

Bushuk, M., and D. Giannakis, 2015: Sea-ice reemergence in a model hierarchy. *Geophys. Res. Lett.*, **42**, 5337–5345, doi:10.1002/2015GL063972.

——, ——, and A. J. Majda, 2014: Reemergence mechanisms for North Pacific sea ice revealed through nonlinear Laplacian spectral analysis. *J. Climate*, **27**, 6265–6287, doi:10.1175/JCLI-D-13-00256.1.

——, ——, and ——, 2015: Arctic sea ice reemergence: The role of large-scale oceanic and atmospheric variability. *J. Climate*, **28**, 5477–5509, doi:10.1175/JCLI-D-14-00354.1.

Cavalieri, D. J., C. Parkinson, N. DiGirolamo, and A. Ivanoff, 2012: Intersensor calibration between *F13* SSMI and *F17* SSMIS for global sea ice data records. *IEEE Trans. Geosci. Remote Sens.*, **9**, 233–236, doi:10.1109/LGRS.2011.2166754.

Chevallier, M., and D. Salas y Mélia, 2012: The role of sea ice thickness distribution in the Arctic sea ice potential predictability: A diagnostic approach with a coupled GCM. *J. Climate*, **25**, 3025–3038, doi:10.1175/JCLI-D-11-00209.1.

——, ——, A. Voldoire, M. Déqué, and G. Garric, 2013: Seasonal forecasts of the pan-Arctic sea ice extent using a GCM-based seasonal prediction system. *J. Climate*, **26**, 6092–6104, doi:10.1175/JCLI-D-12-00612.1.

Coifman, R. R., and S. Lafon, 2006: Diffusion maps. *Appl. Comput. Harmonic Anal.*, **21**, 5–30, doi:10.1016/j.acha.2006.04.006.

Collow, T. W., W. Wang, A. Kumar, and J. Zhang, 2015: Improving Arctic sea ice prediction using PIOMAS initial sea ice thickness in a coupled ocean–atmosphere model. *Mon. Wea. Rev.*, **143**, 4618–4630, doi:10.1175/MWR-D-15-0097.1.

Curry, J. A., J. L. Schramm, and E. E. Ebert, 1995: Sea ice–albedo climate feedback mechanism. *J. Climate*, **8**, 240–247, doi:10.1175/1520-0442(1995)008<0240:SIACFM>2.0.CO;2.

Danabasoglu, G., and Coauthors, 2014: North Atlantic simulations in Coordinated Ocean–Ice Reference Experiments phase II (CORE-II). Part I: Mean states. *Ocean Modell.*, **73**, 76–107, doi:10.1016/j.ocemod.2013.10.005.

Day, J., E. Hawkins, and S. Tietsche, 2014a: Will Arctic sea ice thickness initialization improve seasonal forecast skill? *Geophys. Res. Lett.*, **41**, 7566–7575, doi:10.1002/2014GL061694.

——, S. Tietsche, and E. Hawkins, 2014b: Pan-Arctic and regional sea ice predictability: Initialization month dependence. *J. Climate*, **27**, 4371–4390, doi:10.1175/JCLI-D-13-00614.1.

Gent, P. R., and Coauthors, 2011: The Community Climate System Model version 4. *J. Climate*, **24**, 4973–4991, doi:10.1175/2011JCLI4083.1.

Germe, A., M. Chevallier, D. Salas y Mélia, E. Sanchez-Gomez, and C. Cassou, 2014: Interannual predictability of Arctic sea ice in a global climate model: Regional contrasts and temporal evolution. *Climate Dyn.*, **43**, 2519–2538, doi:10.1007/s00382-014-2071-2.

Giannakis, D., and A. J. Majda, 2012a: Comparing low-frequency and intermittent variability in comprehensive climate models through nonlinear Laplacian spectral analysis. *Geophys. Res. Lett.*, **39**, L10710, doi:10.1029/2012GL051575.

——, and ——, 2012b: Nonlinear Laplacian spectral analysis for time series with intermittency and low-frequency variability. *Proc. Natl. Acad. Sci. USA*, **109**, 2222–2227, doi:10.1073/pnas.1118984109.

——, and ——, 2013: Nonlinear Laplacian spectral analysis: Capturing intermittent and low-frequency spatiotemporal patterns in high-dimensional data. *Stat. Anal. Data Min.*, **6**, 180–194, doi:10.1002/sam.11171.

Guemas, V., M. Chevallier, M. Déqué, O. Bellprat, and F. Doblas-Reyes, 2016: Impact of sea ice initialization on sea ice and atmosphere prediction skill on seasonal timescales. *Geophys. Res. Lett.*, **43**, 3889–3896, doi:10.1002/2015GL066626.

Holland, M. M., C. Bitz, E. Hunke, W. Lipscomb, and J. Schramm, 2006a: Influence of the sea ice thickness distribution on polar climate in CCSM3. *J. Climate*, **19**, 2398–2414, doi:10.1175/JCLI3751.1.

——, ——, and B. Tremblay, 2006b: Future abrupt reductions in the summer Arctic sea ice. *Geophys. Res. Lett.*, **33**, L23503, doi:10.1029/2006GL028024.

——, D. A. Bailey, and S. Vavrus, 2011: Inherent sea ice predictability in the rapidly changing Arctic environment of the Community Climate System Model, version 3. *Climate Dyn.*, **36**, 1239–1253, doi:10.1007/s00382-010-0792-4.

Jahn, A., and Coauthors, 2012: Late-twentieth-century simulation of Arctic sea ice and ocean properties in the CCSM4. *J. Climate*, **25**, 1431–1452, doi:10.1175/JCLI-D-11-00201.1.

Kalnay, E., and Coauthors, 1996: The NCEP/NCAR 40-Year Reanalysis Project. *Bull. Amer. Meteor. Soc.*, **77**, 437–471, doi:10.1175/1520-0477(1996)077<0437:TNYRP>2.0.CO;2.

Koenigk, T., and U. Mikolajewicz, 2009: Seasonal to interannual climate predictability in mid and high northern latitudes in a global coupled model. *Climate Dyn.*, **32**, 783–798, doi:10.1007/s00382-008-0419-1.

Kwok, R., and D. Rothrock, 2009: Decline in Arctic sea ice thickness from submarine and ICESat records: 1958–2008. *Geophys. Res. Lett.*, **36**, L15501, doi:10.1029/2009GL039035.

Large, W., and S. Yeager, 2009: The global climatology of an interannually varying air–sea flux data set. *Climate Dyn.*, **33**, 341–364, doi:10.1007/s00382-008-0441-3.

Lindsay, R., and J. Zhang, 2005: The thinning of Arctic sea ice, 1988–2003: Have we passed a tipping point? *J. Climate*, **18**, 4879–4894, doi:10.1175/JCLI3587.1.

——, and Coauthors, 2012: Seasonal forecasts of Arctic sea ice initialized with observations of ice thickness. *Geophys. Res. Lett.*, **39**, L21502, doi:10.1029/2012GL053576.

Maslanik, J., C. Fowler, J. Stroeve, S. Drobot, J. Zwally, D. Yi, and W. Emery, 2007: A younger, thinner Arctic ice cover: Increased potential for rapid, extensive sea-ice loss. *Geophys. Res. Lett.*, **34**, L24501, doi:10.1029/2007GL032043.

——, J. Stroeve, C. Fowler, and W. Emery, 2011: Distribution and trends in Arctic sea ice age through spring 2011. *Geophys. Res. Lett.*, **38**, L13502, doi:10.1029/2011GL047735.

Maykut, G. A., 1978: Energy exchange over young sea ice in the central Arctic. *J. Geophys. Res.*, **83**, 3646–3658, doi:10.1029/JC083iC07p03646.

Merryfield, W., W.-S. Lee, W. Wang, M. Chen, and A. Kumar, 2013: Multi-system seasonal predictions of Arctic sea ice. *Geophys. Res. Lett.*, **40**, 1551–1556, doi:10.1002/grl.50317.

Msadek, R., G. Vecchi, M. Winton, and R. Gudgel, 2014: Importance of initial conditions in seasonal predictions of Arctic sea ice extent. *Geophys. Res. Lett.*, **41**, 5208–5215, doi:10.1002/2014GL060799.

Owens, W. B., and P. Lemke, 1990: Sensitivity studies with a sea ice–mixed layer–pycnocline model in the Weddell Sea. *J. Geophys. Res.*, **95**, 9527–9538, doi:10.1029/JC095iC06p09527.

Packard, N. H., J. P. Crutchfield, J. D. Farmer, and R. S. Shaw, 1980: Geometry from a time series. *Phys. Rev. Lett.*, **45**, 712–716, doi:10.1103/PhysRevLett.45.712.

Perovich, D. K., and C. Polashenski, 2012: Albedo evolution of seasonal Arctic sea ice. *Geophys. Res. Lett.*, **39**, L08501, doi:10.1029/2012GL051432.

Peterson, K. A., A. Arribas, H. Hewitt, A. Keen, D. Lea, and A. McLaren, 2015: Assessing the forecast skill of Arctic sea ice extent in the GloSea4 seasonal prediction system. *Climate Dyn.*, **44**, 147–162, doi:10.1007/s00382-014-2190-9.

Rigor, I. G., and J. M. Wallace, 2004: Variations in the age of Arctic sea-ice and summer sea-ice extent. *Geophys. Res. Lett.*, **31**, L09401, doi:10.1029/2004GL019492.

Rothrock, D. A., Y. Yu, and G. A. Maykut, 1999: Thinning of the Arctic sea-ice cover. *Geophys. Res. Lett.*, **26**, 3469–3472, doi:10.1029/1999GL010863.

Sauer, T., J. A. Yorke, and M. Casdagli, 1991: Embedology. *J. Stat. Phys.*, **65**, 579–616, doi:10.1007/BF01053745.

Serreze, M. C., M. M. Holland, and J. Stroeve, 2007: Perspectives on the Arctic's shrinking sea-ice cover. *Science*, **315**, 1533–1536, doi:10.1126/science.1139426.

Sigmond, M., J. Fyfe, G. Flato, V. Kharin, and W. Merryfield, 2013: Seasonal forecast skill of Arctic sea ice area in a dynamical forecast system. *Geophys. Res. Lett.*, **40**, 529–534, doi:10.1002/grl.50129.

Stroeve, J., T. Markus, L. Boisvert, J. Miller, and A. Barrett, 2014: Changes in Arctic melt season and implications for sea ice loss. *Geophys. Res. Lett.*, **41**, 1216–1225, doi:10.1002/2013GL058951.

Tietsche, S., and Coauthors, 2014: Seasonal to interannual Arctic sea ice predictability in current global climate models. *Geophys. Res. Lett.*, **41**, 1035–1043, doi:10.1002/2013GL058755.

Vautard, R., and M. Ghil, 1989: Singular spectrum analysis in nonlinear dynamics, with applications to paleoclimatic time series. *Physica D*, **35**, 395–424, doi:10.1016/0167-2789(89)90077-8.

Wang, W., M. Chen, and A. Kumar, 2013: Seasonal prediction of Arctic sea ice extent from a coupled dynamical forecast system. *Mon. Wea. Rev.*, **141**, 1375–1394, doi:10.1175/MWR-D-12-00057.1.

Winton, M., 2006: Does the Arctic sea ice have a tipping point? *Geophys. Res. Lett.*, **33**, L23504, doi:10.1029/2006GL028017.

Wu, B., J. Wang, and J. E. Walsh, 2006: Dipole anomaly in the winter Arctic atmosphere and its association with sea ice motion. *J. Climate*, **19**, 210–225, doi:10.1175/JCLI3619.1.

Yang, Q., S. N. Losa, M. Losch, X. Tian-Kunze, L. Nerger, J. Liu, L. Kaleschke, and Z. Zhang, 2014: Assimilating SMOS sea ice thickness into a coupled ice–ocean model using a local SEIK filter. *J. Geophys. Res. Oceans*, **119**, 6680–6692, doi:10.1002/2014JC009963.